Journal of Applied Polymer Science

Fabrication and Characterization of *In Situ* Synthesized Iron Oxide-Modified Polyimide Nanoweb by Needleless Electrospinning

Naintara Jain,[1] Joy Chakraborty,[1] Santosh Kumar Tripathi,[1] Mohammed Nasim[2]
[1]Defence Materials & Stores R & D Establishment (DMSRDE), Kanpur, Uttar Pradesh, India
[2]Defence Institute of Bio-Energy Research, Goraparao, Haldwani, Nainital, Uttarakhand, India
Corresponding to: M. Nasim (E-mail: nasim_gfast@yahoo.co.in).

ABSTRACT: A series of poly(amic acid) (PAA) solutions were prepared by sol–gel condensation of 4,4′-oxydianiline (ODA) and 4,4′-oxydiphthalic anhydride (ODPA), containing various wt % (5, 10, 15) of an iron oxide precursor, that is, tris(acetylacetonato)iron(III) complex. The resulting PAA solutions were electrospun at 78 kV and collected as webs of nonwoven nanofibers of diameter ~60–70 nm and subsequently converted to iron oxide-modified polyimide (PI) nanofibers by slow thermal imidization. Aminopropyl triethoxysilane (APTES) and tetraethoxyorthosilicate (TEOS) were used as coupling agent and silica precursor, respectively, to enhance the compatibility between organic polymer matrix and inorganic moieties. SEM images reveal smooth and defect-free surface morphologies of the nanofibers. Superparamagnetic properties of the nanofibers were revealed by vibrating sample magnetometer (VSM). FT-infrared spectroscopy (IR), powder XRD, thermogravimetric analysis, and differential scanning calorimetry were employed to systematically characterize material structural properties, thermal stabilities, etc. Nanowebs showed excellent thermal stability around 446°C, with a glass transition temperature around 270°C. The above study demonstrates a good example for fabrication of highly thermally stable bead-free nanofiber webs by needleless electrospinning. © 2014 Wiley Periodicals, Inc. J. Appl. Polym. Sci. **2014**, *131*, 40432.

KEYWORDS: electrospinning; microscopy; nanostructured polymers; polyimides; properties; characterization

Received 4 October 2013; accepted 13 January 2014
DOI: 10.1002/app.40432

INTRODUCTION

Recent advances in nanotechnology as a rapidly growing multidisciplinary field of research have enabled material fabrication and processing at nanoscale because materials in the form of nanofiber not only lead to superior functions but also provide a superior channel to translate it to higher order structures. Unfortunately, ultrafine nanofibers cannot be produced by conventional spinning techniques such as melt spinning, dry spinning, or wet spinning in which micron-sized fibers are generally obtained.[1] Hence, electrospinning has emerged as a feasible low-cost alternative to fabricate continuous nanofibers, and fibers produced this way can also be reinforced by nanoparticles[2] of different metal oxides to generate a composite with unique and tailor-made properties suitable for a wide variety of applications including semipermeable functional membranes,[3,4] filters,[5] protection clothing,[6] surface coatings, conductive composites, biomedical applications such as wound dressing, tissue engineering scaffolds, photocatalysts, biosensors, EMI shielding, and nanoelectronics.[7] Significant progress has been made in the production of ultrafine electrospun nanofiber mats from various types of synthetic and natural polymers having high surface-to-volume ratio.[8] In this direction, aromatic polyimides (PIs) have been well explored as polymer matrix for nanofiber production due to their excellent thermal stability, superior electromechanical properties, and chemical inertness.[9] Several groups have reported PI nanofibers based on pyromellitic dianhydride (PMDA) and 4,4′-oxydianiline (ODA) with ultralow dielectric constant using electrospinning.[10,11] Furthermore, considerable efforts have been given to tailor the properties of such electrospun nanofibers with the incorporation of various metal oxides such as TiO_2, SnO_2, AgO, iron oxide, etc., through surface functionalization of fiber or bulk mixing in order to get improved desired properties for various applications. Interesting features have been observed when the PI has been loaded with magnetic materials,[12–15] making them as polymer magnetic composites, which are supposed to have applications such as memory devices, magnetic fluids, and magnetic sensors. It is possible to produce metal oxide-based, high-functionality polymeric composite nanofibers by the incorporation of metal oxide nanoparticles through electrospinning process in typically three different synthetic routes: deposition, infusion, and *in situ* reaction. Majority of the reports are based on the first two methods, that is, electrospinning of a polymer/polymer precursor solution mixed with different nature or weight percentage of metal oxides.[16,17]

The last method, although less explored, is based on electrospinning of a polymer/metal oxide precursor solution and the post treatment of the produced nanofibers to form desired nanocomposites. This method is becoming popular day by day due to easier *in situ* synthesis, better dispersibility, reduced particle size, and therefore enhanced compatibility with the matrix leading to greater stability and improved performance.[18–20]

Several authors have reported the *in situ* synthesis of iron oxides in polymeric materials especially in PI matrix of 3,3′,4,4′-benzophenonetetracarboxylic acid dianhydride, 1,2,4,5-benzenetetracarboxylic acid dianhydride (PMDA), 2,5-dicarbomethoxyterephthaloyl chloride with ODA,[21,22] with the focus being on the transformation and decomposition of iron complexes to magnetic iron oxides[23–25]; but the possibility of drawing ultrafine smooth defect-free nanofibers from such doped polymeric matrix has remained a field largely unexplored except some research groups such as Panels et al. who in 2008 reported synthesis and characterization of magnetically active carbon nanofiber/iron oxide composites with hierarchical pore structure using polyacrylonitrile as matrix.[20] To explore the feasibility of fabrication of electrospun nanofibers and a comparative study on their properties, a series of PI precursor solutions in DMAc were chosen with varying wt % (5, 10, and 15) of iron oxide precursor as dopant, which decomposes around 190°C to transform into corresponding iron oxide during thermal imidization. APTES (1% of the total solid content of the PAA) was used as a coupling agent and 5% acid hydrolyzed tetraethoxyorthosilicate (TEOS) was added. The presence of pendant APTES groups on the PI facilitates chemical bonding with the partially hydrolyzed alkoxide sol through condensation reactions. Final thermal treatment promotes additional conversion of the alkoxide domains, thus enhancing the compatibility between the organic polymeric chain and its inorganic counterpart to facilitate a hybrid organic–inorganic framework (HOIF) with better thermal stability.

Herein, we present our effort in fabrication of nanofibers by needleless electrospinning of a solution of poly(amic acid) (PAA) prepared from sol–gel condensation of ODPA and ODA mixed with iron oxide and silica precursor. The fibers so generated were subsequently thermally imidized to obtain PI nanofiber mats incorporated with *in situ*-generated metal oxide nanoparticles. The surface morphology of the nanofibers were thoroughly examined using FESEM while other material properties were investigated using FT-infrared spectroscopy (IR), EDAX Dot mapping, rheometer, powder XRD, TGA, DSC, etc., and the magnetic behavior was studied using R.T. VSM.

EXPERIMENTAL

Materials

ODA (97%) and 4,4′-oxydiphthalic anhydride (ODPA, 97%) were commercially obtained from Sigma-Aldrich Chemicals Pvt. Ltd. and purified through vacuum sublimation above their gasification temperature before use. The iron oxide precursor, tris(acetylacetonato)iron(III) (97%, Sigma-Aldrich Chemicals Pvt. Ltd.), APTES (98%, Fluka Analytical), TEOS (98%, Sigma-Aldrich Chemicals Pvt. Ltd.) were used as received. N,N-dimethylacetamide (DMAc, analytical reagent grade, E. Merck, India) was dried with P_2O_5 and vacuum distilled. The solvent was stored with 4Å molecular sieves. All other reagents used were of analytical grade and used as received without further purification.

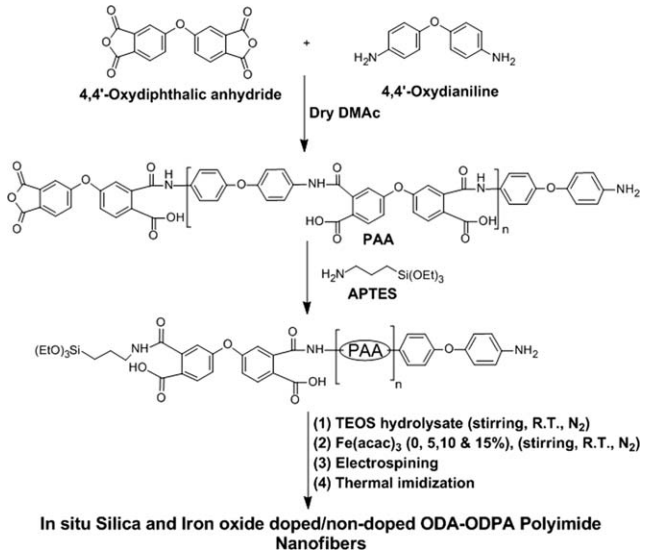

Scheme 1. Synthetic route to iron oxide and silica doped/non-doped polyimide nanofibers.

METHODS

Preparation of Poly(amic acid) Solutions

PAA containing iron oxide precursor was prepared schematically as shown in Scheme 1. The polymerization was conducted in a dry nitrogen-flushed three-necked round bottom flask fitted with a mechanical stirrer for several hours. Crushed ODPA powder (31.02 g) was slowly added to ODA (20.02 g) dissolved in dry DMAc (325 ml) as per literature procedure[21] maintaining the molar ratio of ODPA : ODA = 1 : 1. Reaction mixture was stirred for 2 h at 0°C and then at 25°C for another 15 h in inert atmosphere. APTES (0.54 mL) was added dropwise with continuous stirring for 4 h. *In situ* acid hydrolysis and condensation were carried out by adding the stoichiometric amount of TEOS (13.1 mmol), distilled water (52.4 mmol), and HCl (2.62 mmol). The resulting solution was stirred further at room temperature for 4 h. A clear viscous pale yellow solution of PAA with 15.50 wt % solid content was obtained and subsequently used for the electrospinning experiment. Different wt % (5, 10, and 15) of the dopant, that is, iron oxide precursor and iron (III) acetylacetonate were added to the weighed PAA, and the resultant ruby red colored suspension was stirred thoroughly for 4 h at room temperature under inert atmosphere to avoid fast hydrolysis. Undoped pristine PAA solution was labeled as PI-1, whereas the modified PAA solutions with 5, 10, and 15 wt % of the precursor complex were designated as PI-2, PI-3, and PI-4, respectively.

Needleless Electrospinning of Nanofibers

Needleless electrospinning was carried out at ambient temperature using a nanospider machine (Series: NS Lab 200S Elmarco Nano for Life system, Czech Republic) as per the arrangement shown in Scheme 2. Doped/nondoped PAA solution was fed into a specialized holder containing the rolling spinneret of

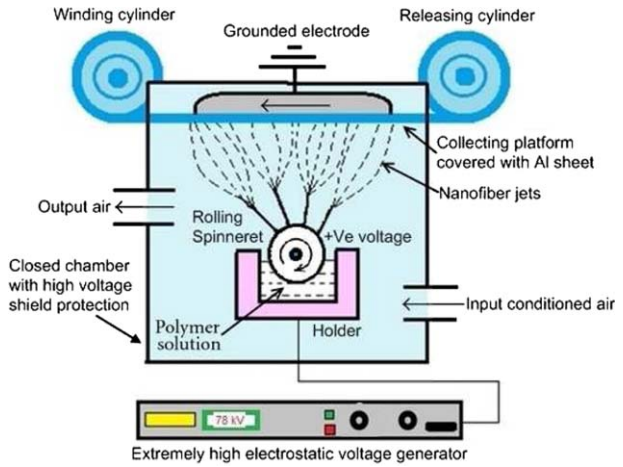

Scheme 2. Schematic process diagram of needleless roller electrospinning. [Color figure can be viewed in the online issue, which is available at wileyonlinelibrary.com.]

diameter 20 mm and length 145 mm. A rotating collector covered with aluminum sheet was placed above and electrically grounded. The spinneret-collector distance was fixed at 180 mm. The speed of the spinneret was kept at 6 rpm because the higher rotation speed led to the breakage of the nanofibers. The slowly rotating spinneret was partially immersed into the polymer solution filled in the holder. Every time the spinneret rotates, it carries an appreciable amount of solution with it to the exposed surface due to surface tension. A very high positive voltage of about 78 kV is applied to the solution. In the presence of such a high electrostatic voltage, the surface of the liquid exposed to the field got distorted into a conical shape usually known as Taylor cone. Once the voltage exceeded a critical value, the electrostatic force outweighed the solution surface tension and stable liquid jets were simultaneously ejected from such various Taylor cone tips so formed on the exposed surface of the rolling spinneret. As these jets traveled through air following the electric lines of force, solvent evaporated leaving behind ultrafine nanofibers collected on the negatively charged rotating collector. The jet often followed a bending or a spiral track resulting from the interaction between the external electric field and the surface charge of the jet. Initially some nanofibers were found entangled and could not be differentiated individually because of the fast jet of the fibers and traction of the rotating collector. The spinning process parameters were optimized with respect to spinnability, regularity of nanofiber layer, and time-related process stability, that is, spinneret rpm, spinneret-collector distance, temperature, and voltage difference. The whole spinning was performed in air and the resulting nanofibers were dried under vacuum at 60°C to remove the residual solvent.

Imidization of Nanofibers

Thermal imidization of the as-spun PAA nanofibers was performed through stepwise heating in a microprocessor-controlled programmable oven in the following sequence: 100 (0.5 h), 150 (0.5 h), 200 (1 h), 250 (2 h), and 300°C (2 h) maintaining the heating rate of 1°C/min in each ascending step. A slow rate of heating ensures removal of residual solvent and the completion of cyclodehydration reaction to form PI, otherwise the water liberated during imidization may cause the deleterious reverse hydrolysis cycle repeat. At this stage, few nanofibers were found partially fused with each other during high-temperature imidization process leading to entanglement in some zones. Hence, the heating rate was adjusted to a minimum value.

Characterization

FTIR spectrum was taken on a Perkin-Elmer Spectrum RXI FTIR Spectrophotometer between 4000–400 cm^{-1}. Thermogravimetric analysis was performed using a TA instrument, USA (TGA-2950) TG-analyser under N_2 atmosphere, at a heating rate of 10°C/min from ambient to 800°C. Differential scanning calorimetric analysis was conducted with TA instrument, USA (TA 2920 DSC) under N_2 atmosphere, at a heating rate of 10°C/min from ambient to 300°C. Surface morphology and structures of the fibers were observed using a field-emission scanning electron microscope (FESEM), Model: Carl Zeiss, Germany, Supra 40 VP. Chemical compositional analysis of the material was performed with an EDAX system (Oxford Instruments, UK), where an incident electron beam of energy between 3–30 keV had been used in an orientation normal to the sample surface. The PI nanofibers were characterized by powder XRD using a Seifert (Isodebyeflex 2002) X-ray generator equipped with Intel CPS-120 high-resolution position sensitive detector and using single monochromatic wavelength of Cu-Kα ($\lambda = 1.54060$Å) as target. The dynamic viscosities of doped and nondoped PAA solutions were measured in DMAc using a TA instrument, USA (AR-G2 Rheometer), at 25°C. Variation of magnetization with the volumetric load of the dispersed inorganic nanoparticles was studied using room temperature magnetization measurements in a Princeton Applied Research model 155 Vibrating Sample Magnetometer (VSM) unit with a maximum magnetic field of 2.1 Tesla and a sensitivity of 10^{-5} emu. Measurements were taken from 0 kOe applied magnetic field to ±2 kOe fields. Necessary diamagnetic corrections were also taken care of.

RESULTS AND DISCUSSION

Scanning Electron Microscopy Studies

The diameter uniformity and preparation of the bead-free electrospun nanofibers are important and required for the fabrication of the membranes used in the sensors, and the surface morphology majorly depends on the viscosities of the polymer solutions as well as the electrospinning conditions (current, voltage, spinneret–collector distance, etc.). All these experimental factors were optimized to ensure defect-free smooth nanofibers in the form of nonwoven web as shown in the typically representative scanning electron micrographs. A total of four numbers of electrospinning reactions were carried out. Figure 1(a) shows the FESEM micrograph of the white nonaligned nanofiber web made of the neat PI (PI-1) and Figure 1(b–d) correspond to three brown-colored webs of the PI doped with iron precursor at different concentrations of 5% (PI-2), 10% (PI-3), and 15% (PI-4) after curing upto 300°C. All the electrospun fibers are solid in nature as shown by the rupture cross section of a single nanofiber of neat PI (PI-1) at a very high magnification of 2,50,000× in Figure 1(e). Heat treatment

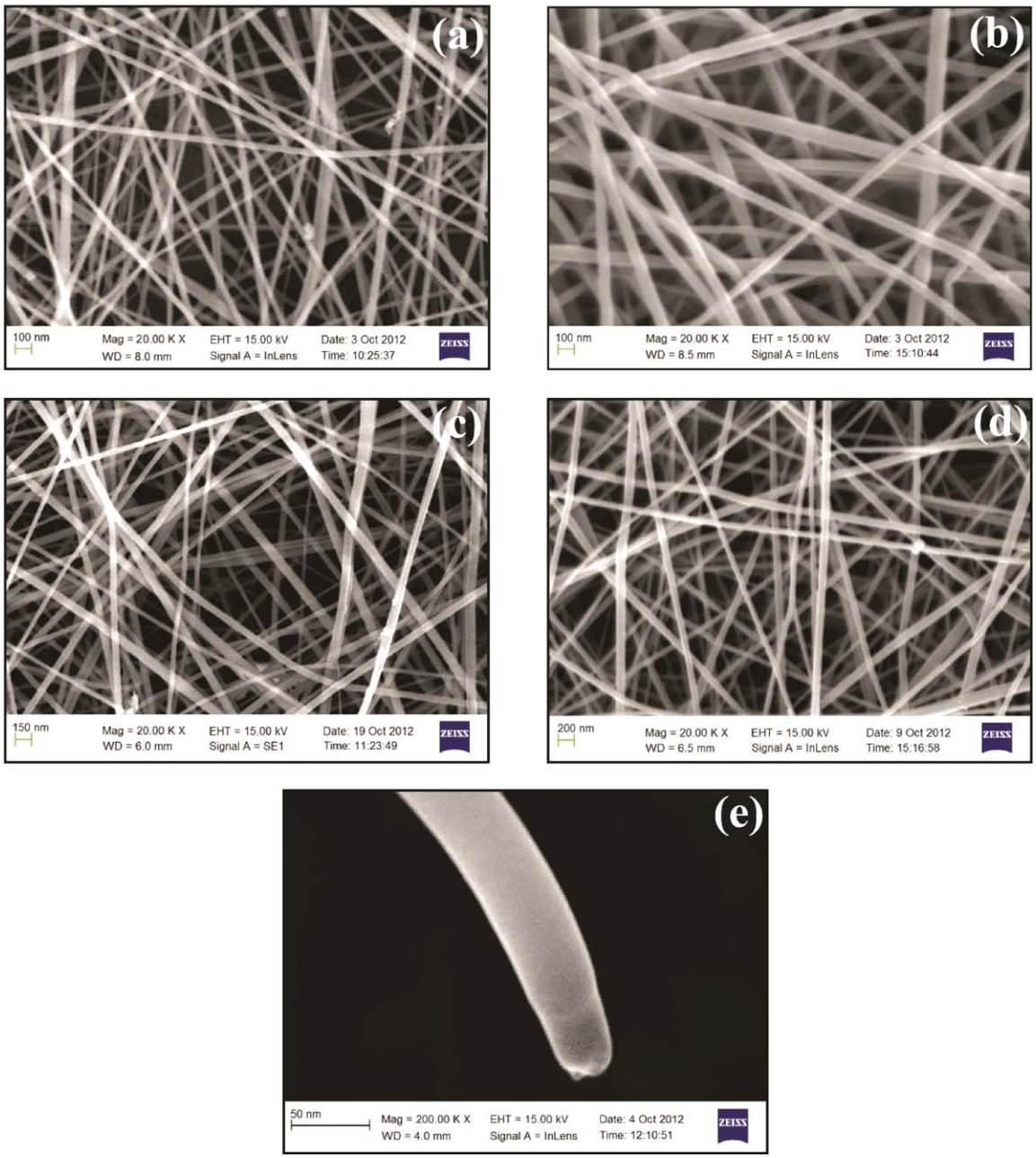

Figure 1. SEM micrographs of (a) PI-1, (b) PI-2, (c) PI-3, (d) PI-4, and (e) high-resolution split end view of a single nanofiber of PI-1. [Color figure can be viewed in the online issue, which is available at wileyonlinelibrary.com.]

during thermal imidization made the fiber surface smoother with a slight decrease in the fiber diameter, suggesting the possibility of densification. However, the nanofibers were found still uniform and continuous after imidization.

The resulting ultrafine nanofibers had a diameter distribution nonuniformly from 50 nm to tens of nm but usually below 230 nm. The surface morphology of a neat PI nanofiber showed a broad distribution in the diameter (~30–60 nm) probably resulting from the unstability of the electrospinning jet, whereas the distribution became narrower and more or less uniform as the inorganic material as a charge carrier is doped in the pristine polyimide due to increasing Coulomb force. The average diameter of the fibers was found in slightly increasing order probably due to the increment in doped viscosity of the PAA solutions.[26] As revealed in the SEM micrographs in Figure 1(b–d), the average diameter of the fibers prepared from the 5 wt % doped PAA solution was found to be ~75 nm, which is almost two and three times smaller in comparison with that of the 10 and 15 wt % solution, that is, ~156 nm and 220 nm, respectively. It is also worth mentioning that adherence of fibers was not observed in any of the cases due to rapid curing of the PAA to PI on the surface of the nanofibers. The packing density of

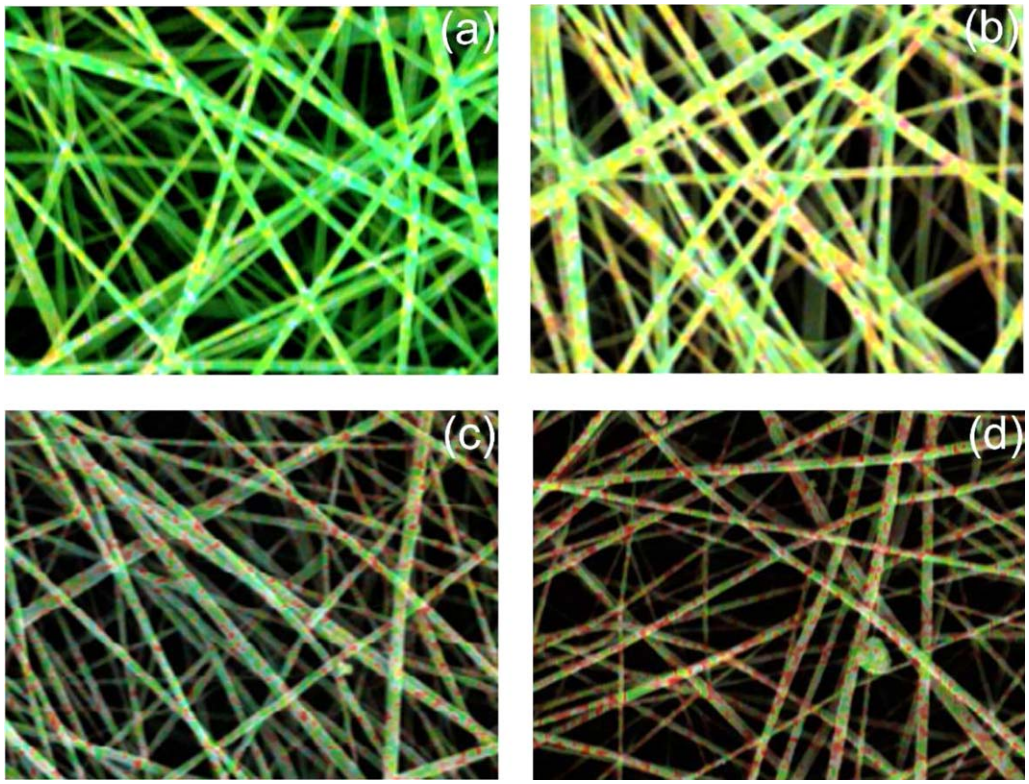

Figure 2. EDAX surface dot mapping images of nanofibers: (a) PI-1, (b) PI-2, (c) PI-3, and (d) PI-4. [Color figure can be viewed in the online issue, which is available at wileyonlinelibrary.com.]

the nanofiber web was found to be increased with take-up speed, which is quite expected as filament tension rises with the former, yielding tighter and more compact nanoweb.

Energy Dispersive X-ray Analysis

Energy dispersive X-ray analysis studies [Figure 2(a–d)] demonstrated that SiO_2 and Fe_2O_3 nanoparticles formed after thermal imidization were homogeneously distributed. The oxide particles so generated did not appear to form clusters or large aggregates, which is a very usual phenomenon especially in case of magnetic oxide particles at increasing particle loading. It invariably points to the advantage of *in situ* process where the particles get a evenly distribution throughout the polymer matrix as well as the particles get encapsulated readily as they form, due to the decomposition of the precursor complex during thermal curing cycle. Iron oxide nanoparticles [Figure 2(b–d)] showed mosaic nanopatterns and nanoparticles were found surrounded by the PI.

Rheological Studies

Rheological analysis was done to correlate between the viscosity and the diameter of the electrospun nanofibers. Dynamic viscosities of the neat, 5, 10, and 15 wt % PAA solutions were recorded as 0.131, 0.153, 0.342, and 0.395 Pa.S, respectively, at varying shear rate at 25°C. The viscosity of PAA was found increasing gradually with increasing percentage of metal oxide precursor complex as shown in Figure 3. It may happen probably due to the coordination of $Fe(acac)_3$ to the multiple sites of the individual PAA chains primarily through the carboxylate anion from the acid functionality by the loss of one anionic acetylacetonate (acac) ligand, thereby crosslinking among polymer chains causing increment in viscosity. It is an usual phenomena observed in case of PAA having multiple free carboxylate ends that can act as chelating sites.[22] Therefore, $Fe(acac)_3$ acts as a crosslinking agent between chains and as iron binds to the free available carboxylate groups of different PAA chains to form a network causing increment in viscosity. It seems that decrement of viscosity by disentanglement of polymer chains was lower than the increment of the same due to the dopant–polymer interactions. Viscosity of the solutions was relatively constant at higher shear rates, which is typical for polymer solutions produced by the sol–gel condensation reactions.[27] The only exception observed in case of PAA solution having 15 wt % dopant. This may be because the precursor when mixed with the PAA in DMAc forms a homogeneous mixture after thorough stirring, hence no shear thinning effect can be expected. But a slight shear thinning effect though observed in the case of PAA solution with highest dopant concentration, that is, PI-4 (15 wt %), may be attributed to the presence of some undissolved particles present in the mixture. The viscosity of the solutions was found proportional to the dopant concentration even at higher shear rates (PI-4 > PI-3 > PI-2 > PI-1). As we know that the electrospinning is always done at higher shear rates, this trend plays a very significant role in doped viscosity of the fed solutions, which in turn directly affects the average diameter of the electrospun nanofibers,[28] which is well supported by the increment of the average diameter of the fibers in an increasing order from neat to 15 wt % dopant as shown in FESEM micrographs.

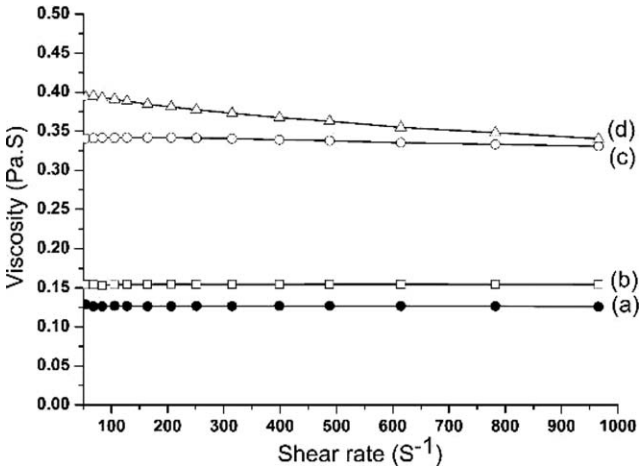

Figure 3. Rheological analyses (viscosity vs. shear rate) of nondoped/doped PAA solutions.

Fourier Transform Infrared Analyses

Infrared spectroscopy continues to be the prominent tool in determining the degree of imidization despite limited agreement on its sensitivity to chemical changes taking place. The chemical structure and complete thermal imidization of PI nanofibers were supported using FTIR spectroscopy as shown in Figure 4. The peak at 1640 cm^{-1} due to ν_{str}(—CONH) of PAA [Figure 4(a)] eventually disappeared and some new peaks appeared in the PI [Figure 4(b)], that is, (i) at 1781 cm^{-1} for ν_{asym}(C═O), (ii) a very sharp and strong band at 1722 cm^{-1} for ν_{sym}(C═O) overlapping with strong carboxylic acid band of ν_{sym}(C═O) at 1700 cm^{-1} of the PAA, (iii) peak at 3487 cm^{-1} due to the (C═O imide) overtone band,[29] (iv) peaks at 1385 and 3556 cm^{-1} due to ν_{str}(C—N), etc.[30] Also, the broad peak appeared around 3636 cm^{-1} may be attributed to the ν_{str}(O—H) probably due to trapped moisture because PIs have a tendency to absorb at least 2% water of its weight.[31] The characteristic bands of SiO_2 can also be seen. Few wide bands appear in the range 1086–1239 cm^{-1} may be correlated to the Si-O-Si bonds while bands at 958 and 829 cm^{-1} can be assigned for Si-OH groups. The FTIR spectrum of iron oxide containing nanofibers in Figure 4(b) shows additional vibrational frequencies around 485 and 563 cm^{-1}, corresponding to the metal oxygen stretching vibration frequencies of Fe_2O_3.[32] There was a slight blue shift in these two peaks compared with the pure Fe_2O_3 possibly due to the weak bonding between PI and Fe_2O_3.

Thermogravimetric Analyses

The TGA curves for virgin (PI-1) and doped (PI-2 to 4) PI nanofibers are shown in Figure 5 and the related data has been presented in Table I. All PI nanofibers experienced majorly two steps mass loss when programmable heating was given under N_2 atmosphere at the heating rate of 10°C/min: (1) Moisture de-trapping: an initial loss (~3%) of mass due to trapped moisture between 60 and 175°C; (2) Carbonization: A major mass loss step (~35%), which commences around 300°C and completes at 614°C, with the maximum decomposition rate (T_{max}) observed at 584, 571, 558, and 553°C for PI-1, PI-2, PI-3, and PI-4, respectively. The polymer decomposition temperatures (PDT, which denotes the temperature at 10% mass loss) were measured using TGA and observed that the introduction of metal oxide into polymer backbones decreased the PDT from 526°C (PI-1, virgin PI) to 486°C (PI-4, 15% iron oxide precursor), only a mere drop of 40°C even after appreciable loading of iron oxide in the matrix. Actually, the iron oxide-modified PI is believed to decompose through an oxidative pathway as the presence of oxygen decreases the PDT of the modified fibers compared with the virgin PI. The oxidative pathway of decomposition is well known to occur through a metal-catalyzed pathway in case of transition metal oxide-doped polymers.[33,34] All the doped nanofibers still displayed impressive thermal stability in inert atmosphere (T_d, thermal decomposition temperature at 5% mass loss: 382–446°C), indicating that the electrospun nanofibers preserve the typical nature of aromatic PI materials. However, no appreciable mass loss was traced in the interval 170–300°C, suggesting complete decomposition of the precursor, that is, $Fe(acac)_3$ to iron oxide during thermal curing. The TGA figure shows that char yield at 800°C increases significantly from 24% (PI-1) to 35% (PI-4) owing to the presence of increasing amount of iron oxide in residue.[35]

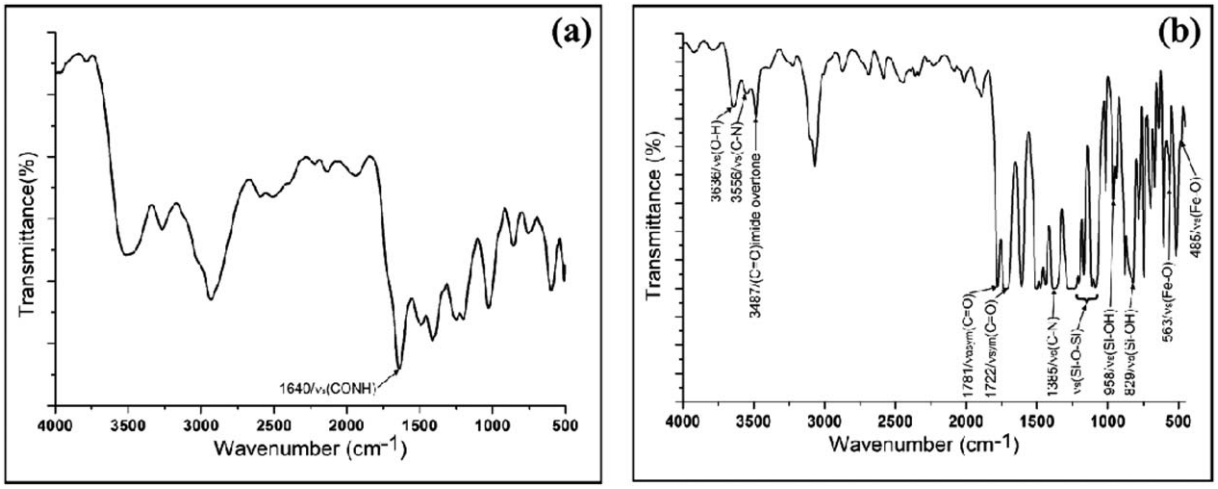

Figure 4. FTIR spectra of (a) virgin PAA and (b) PI-4.

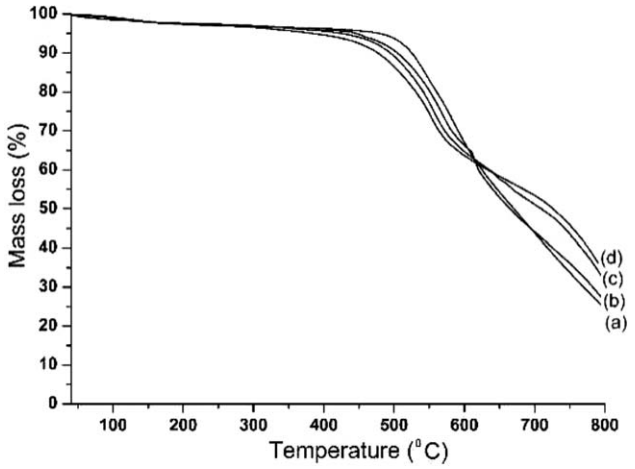

Figure 5. TGA thermograms of doped/nondoped polyimide nanofibers: (a) PI-1, (b) PI-2, (c) PI-3, and (d) PI-4.

Differential Scanning Calorimetry

Figure 6 showed the second heating differential scanning calorimetry (DSC) curves for PI-1 to 4 nanofibers at 10°C/min rate of heating. A broad endothermic hump was observed below 170°C, which was found absent during second heating, suggesting the complete removal of trapped water from the PI nanofibers after first heating. The glass transition temperature (T_g) is evidenced by a step that exhibits onset–inflection–endset points in the DSC curve before sharp melting endotherm. In this case, small characteristic endothermic hump observed above 260°C corresponds to glass transition temperature (T_g) of PIs.[24] Figure 6 shows increment of T_g gradually from 263°C (PI-1, virgin PI) to 277°C (PI-4). The maximum increase as much as 14°C was observed for the doped nanofiber containing 15 wt % precursor, which shows the increasing crystallinity as well as thermal stability of PI nanofibers with increasing percentage of iron oxide nanoparticles in PI matrix. It is very much interesting to note here that T_g showed an upward trend with loading when PDT showed a reverse trend (Table I). Generally, iron oxide nanoparticles reduce the interchain interactions between polymer backbones if physically blended in amorphous PI due to the increase in the geometric freedom of polymer chains, thereby decreasing the glass transition temperature. It is known as confinement effect.[36,37] Although in this case the rigid three-dimensional nature of the *in situ*-generated iron oxide nanoparticles seems to increase the rigidities of the polymer chains to some extent, thereby increasing the T_g. the enthalpic van der Waals interactions between the ultrafine iron oxide nanoparticles so formed play a large role in the efficiency of the stress transfer across the particle/PI interface on heating. This effect along with the strong covalent interaction between the organic polymer chain and the incorporated inorganic SiO_2 moieties due to HOIF gives enough rigidity to the system, hence outweighs the confinement effect to produce resultant increase in the glass transition temperature.[38]

Powder X-ray Diffraction Studies

X-ray powder diffraction is a powerful tool in the monitoring of a synthesis process, as it can easily distinguish between various newly formed phases compared with that of the starting materials. PXRD analysis of the pristine ODA-ODPA PI and its silica and iron oxide-containing nanofibers were compared in the range of 10–90° to determine the chemical state of the incorporated materials along with an estimation of the average particle size of the same. XRD pattern of the bare ODA-ODPA PI matrix (Figure 7a) showed a broad peak centered at 2θ range 17–20°, indicating a short-range molecular order and relatively low crystalline nature, the characteristic of the aromatic PIs. But this broadness of the peak was not perceptible in the XRD patterns corresponding to PI nanofibers containing inorganic nanoparticles, which may be due to an increase in the crystallinity of the polymer with gradual loading of inorganic nanocrystals in the matrix (Figure 7b). The uneven baseline in all these cases may be attributed to the presence of a larger amount of amorphous polymer component and the pattern with diffused peak structure is typical of nanocrystalline materials. Figure 7b is a representative pattern of PI nanofibers with silica precursors and $Fe(acac)_3$, cured at 300°C for 2 h. The broad peak centered in the range of 20° is due to the host amorphous polymer matrix. Well-resolved and a few broad diffraction peaks of low intensity were observed at 2θ values of 11.8°, 14.8°, 15.9°, 17.5°, 18.9°, 23.2°, and 24.1° corresponding to the (211), (301), (202), (400), (110), (501), and (303) Bragg's reflections, respectively. The *d*-spacing indicates that the structure matches with the structure of SiO_2 in tetragonal crystal system in space group I4(82) with lattice parameters, a and $c = 20.01$, and 13.380Å, respectively (JCPDS Card No. 87–1592). It is also clear that the crystalline nature of the fibers increases with loading of the inorganic nanoparticles inside the matrix. X-ray powder diffraction patterns indicate the presence of γ-Fe_2O_3 (maghemite) and Fe_3O_4 (magnetite) particles in the matrix during the curing process. Diffraction peaks at $2\theta = 18.9°$, 30.0°, 38.4°, 45.3°, and 81.8° may be assigned to the Bragg's reflections from (110),

Table I. Thermal Stability of the Doped/Non-Doped Polyimide Nanofibers

Composition	5 %wt. loss at temp[a]	10 %wt. loss at temp[a]	Char yield[b]	T_{max}[a]	T_g (°C)[c]
PI-1	478	526	24	584	263
PI-2	446	506	26	571	270
PI-3	424	494	31	558	272
PI-4	382	486	35	553	277

[a] (°C)
[b] at 800°C (%)
[c] glass transition temperature determined by DSC.

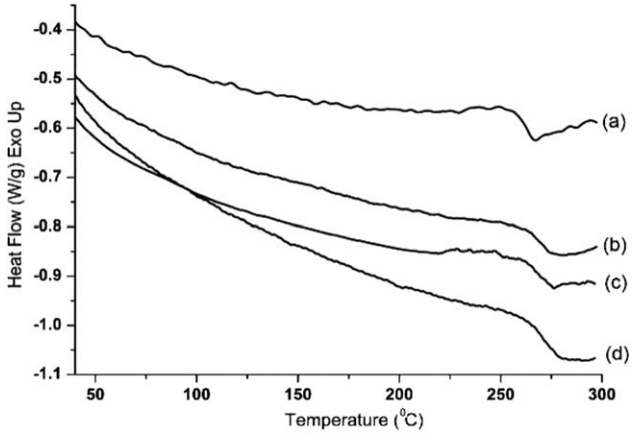

Figure 6. DSC impressions of doped/nondoped polyimide nanofibers: (a) PI-1, (b) PI-2, (c) PI-3, and (d) PI-4.

(210), (220), (311), and (440) planes, respectively. These clearly match with the γ-Fe_2O_3 (maghemite) phase in cubic crystal system in primitive lattice (Space Group: $P_432(213)$) with cell parameters $a = 8.351$Å (JCPDS Card No. 39–1346). Additional weak diffraction peaks of (311), (400), (511), and (440) due to the minor presence of Fe_3O_4 (possibility of remaining unconverted Fe_3O_4 nanoparticles trapped by PI matrix) are smudged by the high-intensity peaks of amorphous PI matrix and could not be resolved to a significant signal-to-noise ratio, leading to some noise like peaks,[39,40] although it can be rationalized in a different way. It was found that the heating of $Fe(acac)_3$ complex to 300°C in air for 1 h produced γ-Fe_2O_3 (maghemite) phase. Also, heating Fe_3O_4 to 300°C under dry air (the same condition in which the nanofiber samples were thermally imidized) generated γ-Fe_2O_3 (maghemite) phase quantitatively. Therefore, if $Fe(acac)_3$ complex was converted to Fe_3O_4 during the thermal imidization, it will be readily oxidized to γ-Fe_2O_3 (maghemite) phase. Furthermore, if FeOOH was produced in the PI matrix during decomposition of the $Fe(acac)_3$ complex, it would readily dehydrate to produce γ-Fe_2O_3 at temperatures above 180°C. WAXS patterns of the samples also did not reveal any trace of other phases of iron oxides, that is, FeO, α-Fe_2O_3, or any hydroxy oxides in the PI matrix as expected. Hence, it is majorly the γ-Fe_2O_3 (maghemite) nanoparticles that seem to be produced *in situ* after thermal imidization of the PI nanofibers at 300°C under dry air for 2 h. There are also observed some extra peaks in Figure 7b, which are reasonably supposed to be due to the decomposition products of the $Fe(acac)_3$ complex, because no such peaks were detected on PI nanofibers without the iron complex. The small particle sizes of nanomaterials contribute to the broadening of the diffraction peaks. If it is assumed that the broadening originates entirely from the small particle size D, the Scherrer's formula[41] predicts that $D = \frac{K\times\lambda}{\beta(2\theta)^c\times\cos\theta}$, where D is the diameter of the particles in nm, λ is the wavelength of the probing X-ray in nm, β is the full width at half maximum in radian, θ is the Bragg's diffraction angle in degree, and $K = 0.94$. The mean crystallite size of the γ-Fe_2O_3 nanoparticles estimated using the above equation is around 24.7 nm. The XRD patterns of the composite nanofibers clearly indicate the changeover from amorphous nature of the pure polymer to that of the partially crystalline state, when iron oxide and silica nanoparticles are present in the matrix, thereby augmenting the crystallinity of the polymer along with a boost in the thermal stability of the system.

Magnetic Studies

Figure 8 shows the magnetic behavior (M vs. H) of the nanofibers at room temperature [PI-1:(a) and samples PI-2 to PI-4:(b-d)], where applied magnetic field was varied gradually from 0 kOe to ±2 kOe. The absence of magnetic hysteresis loop confirms the superparamagnetic nature of the embedded nanoparticles. Remanence is the sample magnetization when the applied magnetic field is zero. Ideally, the coercivity and remanence of superparamagnetic material should be zero. In case of the γ-Fe_2O_3-loaded PI nanofibers, both of the above parameters were found to be zero. It means that there were no magnetic interactions among the nanoparticles in a zero magnetic field environment. It is known that iron oxide clusters with diameter larger than several nanometers exhibit ferromagnetism, although the critical value of the diameter of the clusters changing from superparamagnetic to ferromagnetic depends on the cluster shape and temperature. It is already reported in the literature

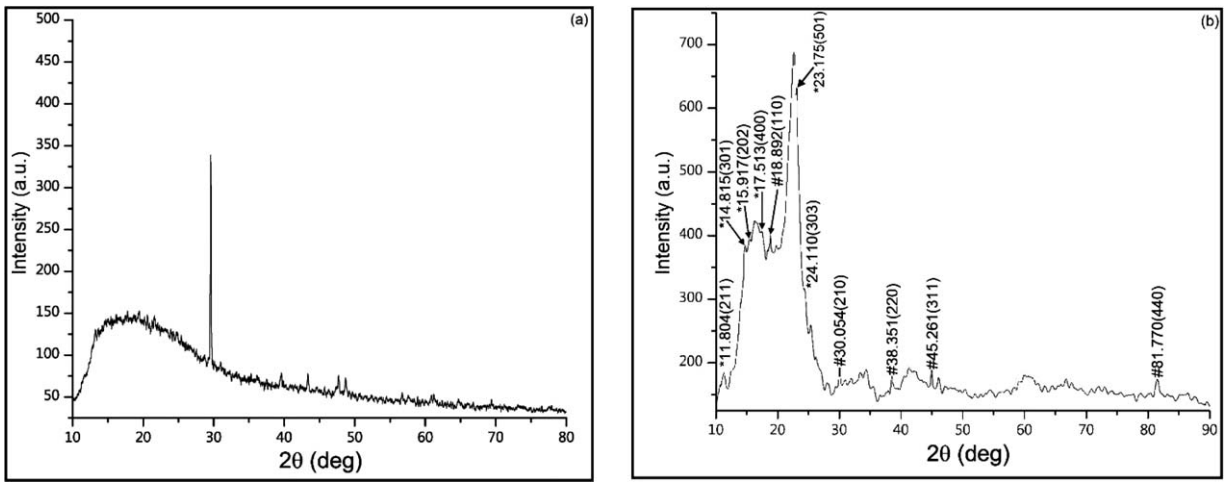

Figure 7. Powder XRD patterns of (a) virgin ODA-ODPA polyimide and (b) PI 4.

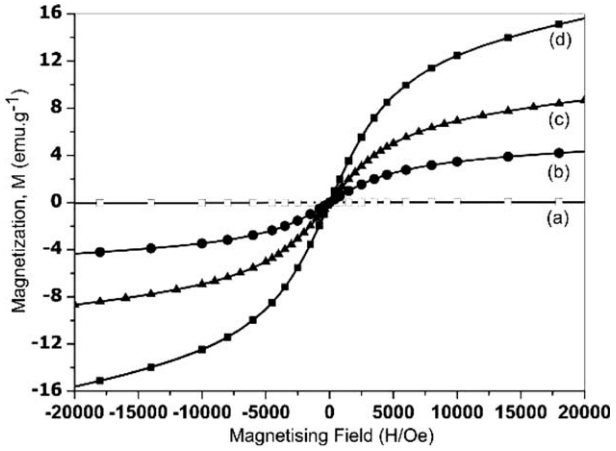

Figure 8. Magnetization (M vs. H) curves of doped/nondoped polyimide nanofibers: (a) PI-1, (b) PI-2, (c) PI-3, and (d) PI-4.

that for ultrafine magnetically ordered particles, there exists a critical size below which the particles can acquire only single magnetic domains even in zero magnetic field. The condition for super-paramagnetism is KV ~ kT, where KV is the anisotropic energy (K, the anisotropic constant; V, the volume of particles, and kT, the thermal agitation energy where k is the Boltzmann constant and T, absolute temperature). When this condition is satisfied, the magnetization of the particles can be excited thermally in unison by the thermal energy kT and can overcome the potential barrier of anisotropy energy, generally referred as super-paramagnetism.[42,43] It is reported that the critical particle size of super-paramagnetism of γ-Fe_2O_3 is about 25 nm. In our case, the average crystallite size of the magnetic nanoparticles has been determined to be around 24 nm, thereby well supporting the above behavior. It can be argued that magnetically significant γ-Fe_2O_3 nanoparticles were encapsulated by PI matrix, therefore their superparamagnetic nature was retained. From the hysteresis curve, it can also be concluded that magnetic properties of the γ-Fe_2O_3-incorporated ODA-ODPA PI nanofibers can be manipulated by changing the concentration of the initial $Fe(acac)_3$ precursor complex, that is, the final loading of γ-Fe_2O_3. With the increasing precursor content from 5% to 15%, the value of saturation magnetization increased from 4 to 16 emu/g. Only silica nanoparticle-incorporated neat PI did not show any magnetic property within the range of investigation giving a saturation magnetization value near to 0 emu/g. Overall, the hysteresis traces of the nanofibers and their scanning electron microscopy images augment each other.

CONCLUSION

Hybrid organic–inorganic PI nonaligned nanofiber web has been successfully fabricated using needleless electrospinning from PAA solution having different concentration of iron oxide precursor, followed by thermal imidization at 300°C. FESEM images revealed smooth and defect-free surface morphology of the nanofibers. Inorganic particles were found to be evenly distributed throughout the polymer matrix as evidenced through EDAX area mapping. Thermal analyses reveal that the nanofibers were highly thermally stable. Incorporation of silica and iron oxide nanoparticles in the PI matrix, by the sol–gel method, brings about considerable enhancement in the compatibility between organic and inorganic phases, which is supported by an increase in glass transition temperature with increasing load of inorganic materials in the matrix. X-ray diffraction identified the phase of iron oxide as maghemite. The study of the effect of iron oxide content on the magnetic property reveals that the nanofibers exhibit typical superparamagnetic behavior, with the remanence and coercivity tending to zero.

ACKNOWLEDGMENTS

N. J. thanks Defence Research and Development Organisation (DRDO), Government of India, Ministry of Defence, for the financial support as a Senior Research Fellowship. Authors also sincerely thank the Director, DMSRDE, Kanpur, for the help in using the infrastructure and full utilization of the resources. Support from the Electron Microscopy Group, Defence Metallurgical Research Laboratory (DMRL), Hyderabad, is also hereby greatly acknowledged.

REFERENCES

1. Kroschwitz, J. I.; Howe-Grant, M. Kirk-Othmer Encyclopedia of Chemical Technology, 4th ed.; Wiley: New York, Vol. 10, **1991**.
2. Hu, N.; Dang, G.; Zhang, H.; Du, Y.; Wang, C.; Zhou, H.; Meng, X.; Chen, C. *J. Nanosci. Nanotech.* **2009**, *9*, 6688.
3. Shin, Y. M.; Hohman, M. M.; Brenner, M. P.; Rutledge, G. C. *Polymer.* **2001**, *42*, 9955.
4. Megelski, S.; Stephens, J. S.; Chase, D. B.; Rabolt, J. F. *Macromolecules* **2002**, *35*, 8456.
5. Tsaia, P. P.; Schreuder-Gibson, H.; Gibson, P. *J. Electrostat.* **2002**, *54*, 333.
6. Schreuder-Gibson, H. L.; Gibson, P.; Senecal, K.; Sennett, M.; Walker, J.; Yeomans, W. *J. Adv. Mater.* **2002**, *34*, 44.
7. Norris, I. D.; Shaker, M. M.; Ko, F. K.; MacDiarmid, A. G. *Synth. Met.* **2000**, *114*, 109.
8. Yang, H.; Loh, L.; Han, T.; Ko, F. Nanomagnetic Particle Filled Piezoelectric Polymer Nanocomposite Wires by Co-electrospinning, American Chemical Society, New York, **2003**.
9. Nah, C.; Han, S. H.; Lee, M.-H. *Polym. Intl.* **2003**, *52*, 429.
10. Liu, J. Y.; Min, Y.; Chen, J. Y.; Jhou, H. W.; Wang, C. *Macromol. Rapid Commun.* **2007**, *28*, 215.
11. Yang, K. S.; Edie, D. D.; Lim, D. Y.; Kim, Y. M.; Choi, Y. O. *Carbon* **2003**, *41*, 2039.
12. Koo, O. M.; Rubinstein, I.; Onyuksel, H. *Nanomed. Nanotechnol. Biod. Med.* **2005**, *1*, 193.
13. Yoon, C. *J. Magn. Magn. Mater.* **2004**, *272–276*, E1167.
14. Boggess, R. K.; Taylor, L. T. *J. Polym. Sci., Polym. Chem. Ed.* **1987**, *25*, 685.
15. Angelo, R. J. E. I. DuPont de Nemours Co.; US Patent, 3,073,785, **1959**.

16. Byung, W. A.; Kang, T. J. *J. Appl. Polym. Sci.* **2012**, *125*, 1567.
17. Jang, J.; Lee, K. J.; Kim, Y. *Chem. Commun.* **2005**, 3847.
18. Hong, Y. L.; Li, D. M.; Zheng, J.; Zou, G. T. *Nanotechnology* **2006**, *28*, 1986.
19. Majidi, R. F.; Sanjani, N. S. *J. Appl. Polym. Sci.* **2007**, *105*, 1351.
20. Panels, J. E.; Lee, J.; Park, K. Y.; Kang, S. Y.; Marquez, M.; Wiesner, U.; Joo, Y. L. *Nanotechnology* **2008**, *19*, 455612.
21. Lv, Y.-Y.; Wu, J.; Wan, L.-S.; Xu, Z.-K. *J. Phys. Chem. C.* **2008**, *112*, 10609.
22. Bergmeister, J. J.; Taylor, L. T. *Chem. Mater.* **1992**, *4*, 729.
23. Okada, H.; Sakata, K.; Kunitake, T. *Chem. Mater.* **1990**, *2*, 89.
24. Nandi, M.; Conklin, J. A.; Salvati, L., Jr.; Sen, A. *Chem. Mater.* **1990**, *2*, 772.
25. Tannenbaum, R.; Goldberg, E. P.; Flenniken, C. L. Metal-Containing Polymeric Systems, Plenum Press, New York, **1985**, 303.
26. Shin, Y. M.; Hohman, M. M.; Brenner, M. P.; Rutledge, G. C. *Appl. Phys. Lett.* **2001**, *78*, 1149.
27. Yang, K. S.; Edie, D. D.; Lim, D. Y.; Kim, Y. M.; Choi, Y. O. *Carbon* **2003**, 2039.
28. McKee, M. G.; Wilkes, G. L.; Colby, R. H.; Long, T. E. *Macromolecules* **2004**, *37*, 1760.
29. Jamal, K.; Ashwani. K. *J. Polym. Sci.* **2006**, *102*, 369.
30. Singh, B. P.; Singh, D.; Mathur, R. B.; Dhami, T. L. *Nanoscale Res. Lett.* **2008**, *3*, 444.
31. Musto, P.; Mascia, L.; Mensitieri, G.; Ragosta, G. *Polymer* **2005**, *46*, 4492.
32. Hiremath, A. V.; Venkataraman, A. *Bull. Mater. Sci.* **2004**, *26*, 391.
33. Aly, M. M.; El-Awad, A. M. *Inorg. Chim. Acta* **1980**, *38*, 3.
34. Bergmeister, J. J.; Rancourt, J. D.; Taylor, L. T. *Chem. Mater.* **1990**, *2*, 640.
35. Tsai, M. H.; Whang, W. T. *Polymer* **2001**, *42*, 4197.
36. Bansal, A.; Yang, H. C.; Li, C. Z.; Cho, K. W.; Benicewicz, B. C.; Kumar, S. K.; Schadler, L. S. *Nat. Mater.* **2005**, *4*, 693.
37. Ash, B. J.; Rogers, D. F.; Wiegand, C. J.; Schadler, L. S.; Siegel, R. W.; Benicewicz, B. C. *Polym. Compos.* **2002**, *23*, 1014.
38. Zhang, Q. L.; Gupta, S.; Emrick, T.; Russell, T. P. *J. Am. Chem. Soc.* **2006**, *128*, 3898.
39. Zhan, J.; Tian, G.; Jiang, L.; Wu, Z.; Wu, D.; Yang, X.; Jin, R. *Thin Solid Films* **2008**, *516*, 6315.
40. Oka, H.; Inagaki, M.; Kaburagi, Y.; Hishiyama, Y. *Solid State Ionics* **1999**, *121*, 157.
41. Patterson, A. L. *Phys. Rev.* **1939**, *56*, 978.
42. Peniche, H.; Osorio, A.; Acosta, N.; de la Campa, A.; Peniche, C. *J. Appl. Polym. Sci.* **2005**, *98*, 651.
43. Kaburagi, Y.; Hishiyama, Y.; Oka, H.; Inagaki, M. *Carbon* **2001**, *39*, 593.